TURBULENCE IN THE ANISOTROPIC BOUNDARY LAYER

V.V. Nosov, V.M. Grigoriev*, P.G. Kovadlo*, V.P. Lukin, E.V. Nosov, A.V. Torgaev
Institute of Atmospheric Optics SB RAS, 1, Akademicheskii ave., Tomsk 634055, Russia
**Institute of Solar-Terrestrial Physics SB RAS, 126, Lermontova str., Irkutsk 664033, Russia*

ABSTRACT

Processes of Benard cell origination and disintegration in air are studied experimentally. It is shown that temperature gradients cause a Benard cell. Our data confirm the main scenarios of turbulence origination (Landau–Hopf, Ruelle–Takens, Feigenbaum, and Pomeau–Menneville stochastic scenarios). It is ascertained that a Benard cell disintegrates according to the Feigenbaum scenario. In this case, the main vortex in the Benard cell is decomposed into smaller ones as a result of ten period-doubling bifurcations. It is shown that the resulting turbulence is coherent and determinate; the fractal character (local self-similarity) of its spectrum is found. These results allow the definition of a coherent structure as a compact formation containing a long-lived three-dimensional hydrodynamic cell (originating from long-term action of thermodynamic gradients) and products of its discrete coherent cascade disintegration. The coherent structure answers all the signs of chaos occurrence (turbulence) in typical thermodynamic systems. On the base of the results, presented in this work, a coherent structure can be considered as a key turbulence element. It is shown that the real atmospheric turbulence is the result of mixing of different coherent structures.

Key words: turbulence, Benard cell, stochastization scenario, coherent structure, random analysis, spectrums

INTRODUCTION

Processes of Benard cell origination and disintegration in air are studied experimentally. It is shown that temperature gradients cause a Benard cell. Our data confirm the main scenarios of turbulence origination (Landau–Hopf, Ruelle–Takens, Feigenbaum, and Pomeau–Menneville stochastic scenarios). It is ascertained that a Benard cell disintegrates according to the Feigenbaum scenario. In this case, the main vortex in the Benard cell is decomposed into smaller ones as a result of ten period-doubling bifurcations. It is shown that the resulting turbulence is coherent and determinate; the fractal character (local self-similarity) of its spectrum is found.

These results allow the definition of a coherent structure as a compact formation containing a long-lived three-dimensional hydrodynamic cell (originating from long-term action of thermodynamic gradients) and products of its discrete coherent cascade disintegration. The coherent structure answers all the signs of chaos occurrence (turbulence) in typical thermodynamic systems. Our results show that known processes of transformation of the laminar flows to turbulent ones (Rayleigh-Benard convection, fluxions in pipes, a fluid flow around hindrances, etc.) are the coherent structures (or sum of such structures). Therefore, it is possible to consider coherent structure a basic element of the turbulence.

Origination of a coherent structure in a closed room follows from the experiments, described in Ref. 1. The most interesting are measurement results of turbulence parameters inside the astronomic spectrograph pavilion of the Large Solar Vacuum Telescope (LSVT)[1]. These results are of primary importance for finding coherent structures. Therefore, in this work (the 1st part) we describe the experiment and its results with necessary additions, following from an analysis of the results with relation to coherent structure origination.

Coherent structures in open air (the 2nd part) are considered using data of other measurements, carried out by the authors in 2000th (see, e.g., Ref. 2). In all these measurements, a mobile ultrasound meteosystem was used; it records more than hundred of atmospheric parameters (with sufficient precision[1, 2]). It is shown that the real atmospheric turbulence is the result of mixing of different coherent structures. It follows from our data, that extended areas are often observed in open air, where one coherent structure exercises a decisively influence. Due to a difference of atmospheric coherent turbulence from the Kolmogorov non-coherent one, the values of Kolmogorov C and Obukhov C_θ constants in the Kolmogorov–Obukhov law are verified. It is shown that the error of their definition can be 93%. This is one of the reasons of large errors in measurements of turbulent atmospheric parameters.

Further author information: nosov@iao.ru

1. COHERENT STRUCTURE IN A CLOSED ROOM

The scheme of measurements in the LSVT spectrograph pavilion is shown in Fig. 1. The pavilion is an isolated big closed rectangular room of about 5 x 16 x 7 m (height, length, width) in size, west-eastward elongate. Inside surfaces of the room is smooth, walls are without windows. There is an entrance (doubled-up) door from the south side and air hole (0.5 m × 0.5 m) in the southwest upper angle of the pavilion. Measurements in the spectrograph pavilion were carried out at two height levels from the floor *h*: the lower level 1.10 m corresponded to the optical path height in the pavilion (points *1–7* in Fig. 1); the height of the upper one was mainly 3.10 m (points *9–12* in Fig. 1, 2.55 m – for point *8*). The entrance door and air hole were closed during the measurements.

A high level of temperature and refraction index fluctuations in the pavilion follows from the measurement results. The intensity of these fluctuations is usually characterized by the structural characteristics C_T^2 and C_n^2. For example, C_n^2 at the lower level (points *1–7*) reaches the value $1.6 \cdot 10^{-14}$ cm$^{-2/3}$. At average, C_n^2 decreases with height.

Noticeable gradients of average temperature $\langle T \rangle$ have been recorded in the pavilion. Thus, the vertical gradient between points *2* and *8* (near the east wall) reaches the value $d\langle T \rangle/dh = -0.41$ deg/m (the average temperature decreases to the top). The value of vertical gradient, averaged over all the observation points in the pavilion, equals –0.145 deg/m. The value of longitudinal horizontal gradient (along the east-westward directed optical path), averaged over all the observation points at the path height 1.1 m, equals –0.028 deg/m (average temperature decreases when transferring from the east to west wall). However, this averaged gradient essentially decreases at the upper measurement level (at a height of 3.1 m) and becomes equal to +0.009 deg/m. Considering the spectrograph-measured temperature gradients, one can see that the pavilion floor, east and west walls are the hottest. A built smoothed vector of pavilion temperature gradient, corresponding to measured vertical and side gradients, is to be a straight line directed from the ceiling near the southwest angle (air hole) to the floor near the northeast angle of the pavilion (alignment table).

Spatial periodicity of some variables (of quincunx structure type) is observed in a vertical plane passing through the optical path in the pavilion (through points *2* and *4–6*). For example, the Monin–Obukhov number alternates in sign, the average temperature periodically deviates from the value, smoothed over the points at one height. The structural characteristics C_T^2 and C_n^2 are periodic at the lower level in this plane. Similar periodicity takes place for the inner and outer turbulence scales. Such behavior of the above parameters connected with origination of stable periodic vortex formations in large closed rooms.

1.1. INCIPIENT CONVECTIVE TURBULENCE. BENARD CELLS

The map of recorded averaged air motion (wind map) inside the pavilion is shown in Fig. 1. Comparatively strong counter wind flows are observable at the lower measurement level in the pavilion centre (approximately, pavilion lengthwise, East–West direction). A similar pattern is observable at the upper measurement level, while the motion speed essentially decreases here and motion directions are displaced toward the air hole. The solid alignment table strongly affects air motion near the east wall, where airflows are mainly directed along and toward the wall.

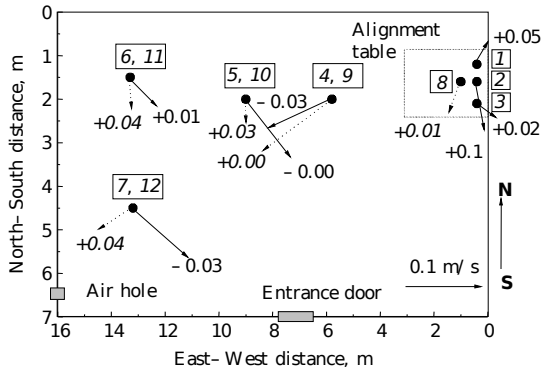

Fig. 1. Spectrograph pavilion. Scheme of measurements in the pavilion (overhead view) and wind map. Numbers inside the rectangles are the numbers of measurement points; numbers near the arrays' ends with the signs «+» or «–» are the values of vertical wind (m/s). Solid arrows and non-italic numbers correspond to the velocity at the floor of pavilion (*1–7*), dashed arrows and italic numbers – at the top of pavilion. The velocity scale is shown in the right bottom angle

It also follows from the obtained data that the sign of Monin-Obukhov number ζ, characterizing the temperature local temperature stratification, alternates in sign at the optical path height when passing from the east pavilion wall to the west one (through points *2* and *4–6*). Similar spatial periodicity is observed for the deviation ΔT ($\Delta T = \langle T \rangle - \langle T \rangle_{av}$) of the average temperature $\langle T \rangle$ from the smoothed average temperature $\langle T \rangle_{av}$, considered as a function of distance in the path through points *2* and *4–6*. Thus, $\zeta = -5.16$, $\Delta T = -0.04$ deg at point *2*; $\zeta = +0.47$,

$\Delta T = +0.29$ grad at point *4*; $\zeta = -4.55$, $\Delta T = -0.07$ deg at point *5*; $\zeta = +0.49$, $\Delta T = +0.06$ deg at point *6*. These results allow us to ascertain the character of averaged flows between observation points and to build a more detailed motion pattern.

Actually, let ΔT exceeds zero at a certain point. This means a higher temperature of air at this point as compared to neighboring adjoining areas at the same level. Warm air is lighter than cold one. Hence, cold air runs under the warm one and displaces it upward. If $\zeta > 0$ at this point, then there is a warmer air over the observation point, which follows from the sense of the parameter ζ, while the air at the point is colder and heavier. Hence, a blocking buoyancy force appears at $\zeta > 0$. Thus, two vertical opposite directed forces affect the air volume at $\Delta T > 0$ and $\zeta > 0$ (stabilizing action of stable stratification competes with destabilizing effect of an unstable temperature profile[3]). These forces restrict vertical travels of air volume and allow only horizontal movements (e.g., at point *4* in Fig. 1). At $\Delta T < 0$ and $\zeta < 0$, the situation is similar (for example, at point *5* in Fig. 1). However, between these areas, when, e.g., $\Delta T > 0$ and ζ changes from positive to negative ($\Delta T > 0$, $\zeta < 0$), both vertical force are directed upward and, hence, the air volume moves upward (gap between points *4* and *5* in Fig. 1). Otherwise ($\Delta T < 0$, $\zeta > 0$), both forces are directed downward and air moves downward. Such situation is probable in the gap between point *2* and *4* and near point *6* in Fig. 1.

A more detailed pattern of air motion in the pavilion in a vertical plane passing through the optical path (through observation points *2* and *4–6*) can be built on the grounds of the above data. Such approximate pattern is shown in Fig. 2. Here the solid slant line shows the (above plane) projection of smoothed average temperature gradient vector.

As is seen from Fig. 2, there are rotating airflows (whirls) into the pavilion. Averaged air motion in the pavilion is similar to vortex toroidal motion of liquid in a space cell, which is the pavilion. The cell axis (torus axis) is parallel to the temperature gradient vector (slant line in Fig. 2). In the pavilion center, air moves up-axis, parallel to the gradient direction, while near the walls – down-axis. Fig. 2 reflects only principal properties of air motion in the pavilion, real motions are more complicated. Artificial obstacles to the flows (mirrors, screen, etc.) distort these vortex flows. It is clear, that circulation of averaged flows is caused by the temperature gradient, existing in the pavilion. These equilibrium vortices, observable in a completely closed room, can be interpreted as Benard convection cells[3].

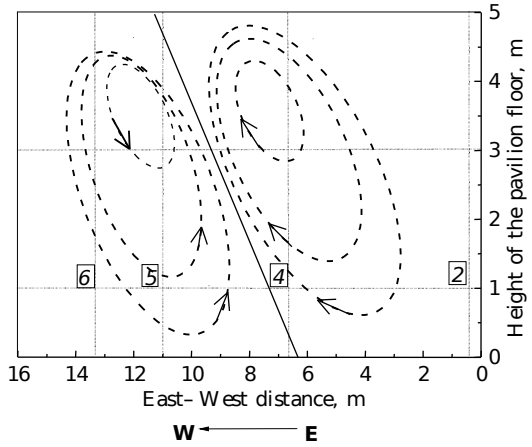

Fig. 2. Air motion inside the pavilion in a vertical plane through points *2* and *4–6* (their positions are designated by italic numbers). Ellipses show the trajectories of averaged motions, slant solid line – the projection of smoothed average temperature gradient

Theoretical models, implying existence of Benard convection cells, were built long ago. It follows from the theory that origination of the cells (to which the convective motion is decomposed) requires a temperature gradient between opposite planes. The cells can take a shape of hexagonal prisms (with an axis along the gradient) depending on the gradient value. In the centre of such prisms, liquid moves up-axis (parallel to the gradient direction) and along the edges – down-axis ($d\nu/dT < 0$, ν is the kinematic viscosity), or *vice versa* ($d\nu/dT > 0$). In more complex (than two space-apart planes) space areas, the cells can take other than hexagonal forms, e.g., longitudinal and transverse-longitudinal rolls (often with neck) etc. Model (vessel) experiments with water, oil, liquid helium as a medium, confirm the fact of origination of Benard convection cells[3]. Such experiments for air inside large closed rooms were not carried out earlier, as they require small detection device sensitive to motion of weak airflows.

As is known[3], origination of Benard cells (stationary periodic motion) requires that the Rayleigh number *Ra* exceed the critical number Ra_{cr}. According to the definition, $Ra = g\beta h^3(T_0 - T_h)/(\nu\chi)$, where T_0 and T_h are the air temperatures at the bottom and on the top of a *h*-height level; *g* is the gravitational acceleration; β is the thermal-expansion coefficient ($\beta = 1/T_0$); ν is the kinematic viscosity; χ is the air thermal diffusivity. Substituting values of the parameters ($T_0 = 285.1$ K; $T_h = T_0 + h\langle T\rangle/dh$, $h = 5$ m, $d\langle T\rangle/dh = -0.145$ deg/m; $\nu = 1.3 \cdot 10^{-5}$ m^2/s, $\nu = 0.7\chi$), obtain $Ra = 1.3 \cdot 10^{10}$. The critical Rayleigh number Ra_{cr} is (according to Ref. 3) within the range 657–1708. Hence, the recorded *Ra* essentially exceeds the critical number ($Ra \gg Ra_{cr}$) and stationary periodic motions exist. Thus, the measurement results (Figs. 1 and 2) confirm the presence of Benard convection cells for averaged motions inside closed rooms.

Theoretical study of stability of liquid motion between two space-apart planes (implies existence of Benard cells) allows several scenarios of turbulence origination (initiation) to be formulated. In particular, it was ascertained[3,4] that the turbulence, originating in closed volumes, is undeveloped in conditions of instability of convective motions. A part of liquid energy is spent for regular (laminar) motions (vortices in Benard cells), another – for turbulent ones. It is clear from this definition that random air motion inside a closed room is an example of incipient turbulence.

Statistical characteristics of the incipient undeveloped turbulence in air are insufficiently studied[3,5]. Therefore, it is interesting to point out some characteristic features of undeveloped turbulence, distinguishing it from the developed turbulence mode. Consider here (as the simplest) structure and correlation functions of temperature fluctuations.

Figures 3 and 4 show the comparison results of experimental data for main statistical characteristics of air temperature fluctuations in a closed room and in open air. For a closed room, data correspond to measurements in point *5* inside the spectrograph pavilion ($\zeta = -4.5$, $C_n^2 = 1.6 \cdot 10^{-14}$ cm$^{-2/3}$, $h = 1.1$ m, $\langle T \rangle = 11.95$ deg, $V = 0.09$ m/s). For open air, typical experimental data were chosen. They were obtained separately in summer measurements over an approximately flat underlying surface in the clear dry weather ($\zeta = -3.8$, $C_n^2 = 6.5 \cdot 10^{-16}$ cm$^{-2/3}$, $h = 3.1$ m, $\langle T \rangle = 24.56$ deg, $V = 0.86$ m/s).

As is evident from Fig. 3, which shows two-minute realizations of random temperature, the random fluctuation process in the open air is close to a steady-flow one. In closed room conditions, fluctuation process is clearly divided into two intervals with different turbulence modes, one of which changes another one with discrete jump. The jump shows an appearance of a steady flow from the previous one, with new characteristics. This phenomenon is called bifurcation of stability change[3].

As is follows from Fig. 4, the structure functions of temperature fluctuations $D_T(\tau)$ at small time intervals τ are Kolmogorov functions ($D_T \sim \tau^{2/3}$) both in developed and undeveloped turbulence. At large time intervals, they essentially differ. The fluctuation correlation coefficient b_T inside a closed room has a number of sufficiently large local maxima, in contrast to open air. Each such maximum meets a local minimum of the structure function D_T (their arguments agree). The structural function $D_T(\tau)$ at very small τ in a closed room has a quadratic segment (see Fig. 4, bottom left subfigure), longer than in open air, which corresponds to increased values of the inner turbulence scale.

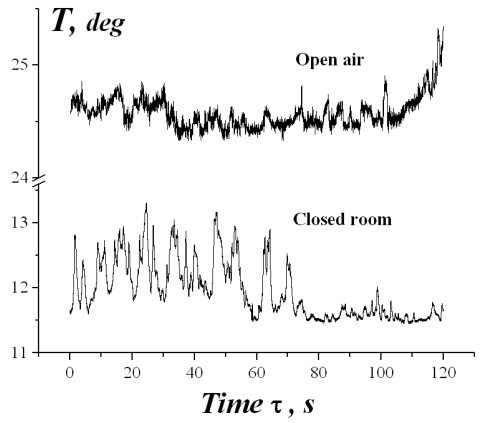

Fig. 3. Two-minute realizations of the random temperature T in a closed room and in open air

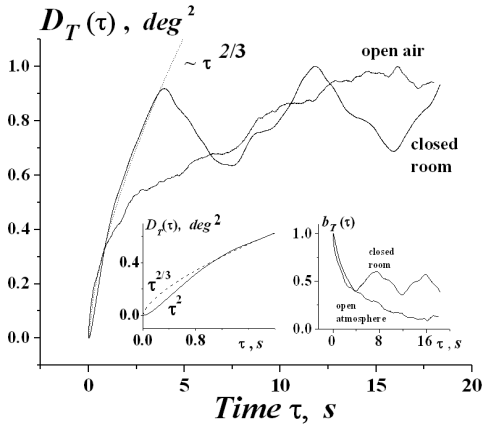

Fig. 4. Normalized structure $D_T(\tau)$ and correlation $b_T(\tau)$ (right bottom subfigure) functions in a closed room and in open air (the initial segment of $D_T(\tau)$ is shown at the bottom left)

1.2. MODELS OF TEMPERATURE FLUCTUATION SPECTRA IN THE INCIPIENT TURBULENCE

Models of temperature fluctuation spectra, first of all, of the spatial 3D spectrum $\Phi_T(\iota)$, are required in problems of optical radiation propagation in undeveloped turbulence.

As is known[5], time frequency spectra of temperature fluctuations $W_T(f)$ in open air are adequately described by the Karman model. The Kolmogorov developed turbulence spectra have a long inertial interval, where $W_T \sim f^{-5/3}$ and the energy is transported from large-scale vortices to smaller ones.

Smoothed time frequency spectra of temperature fluctuations W_T are shown in Fig. 5 for a closed room (point *5* in Fig. 1) and open air. As is seen, the closed-room spectra roll-off much more rapidly than open-air ones within the inertial interval; besides, within the interval, there are only short individual frequency regions (in echelon), inside which the turbulence can be considered as Kolmogorov ($W_T \sim f^{-5/3}$). These regions are observed between jumps of the spectral function at the frequencies, corresponding to local maxima of fluctuation correlation function (or minima of the structure function). In case of smoothed echelons, experimental spectra of undeveloped turbulence have a number of characteristic regions of rapid power decrease. Thus, if $W_T \sim$ const at a long energy interval, then first $W_T \sim f^{-8/3}$ with frequency rise (within the inertial interval) and then $W_T \sim f^{-12/3}$. Hence, energy transport from large to small vortices is insignificant in the incipient turbulence, i.e., the vortices are weakly diffused. Spectra roll-off slows down ($W_T \sim f^{-2/3}$) with further frequency rise, in the viscous interval, where the spectral density is close to the noise level. Similar behavior of spectra is observed at other points of the pavilion. The spectrum echelon is pronounced even stronger at some points.

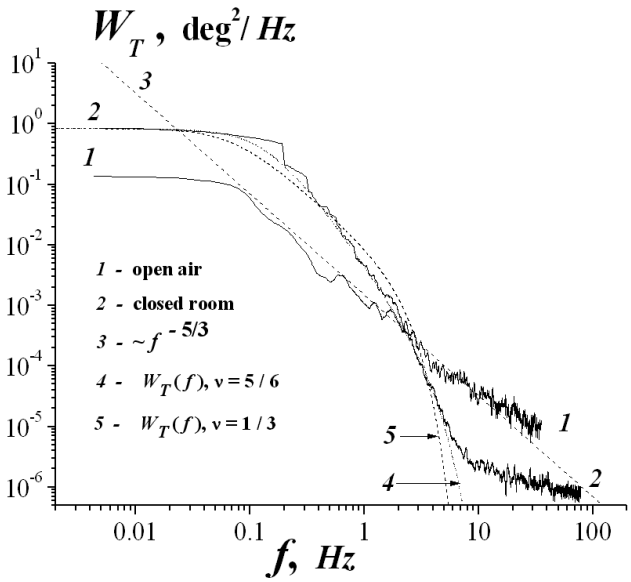

Fig. 5. Smoothed time frequency spectra of temperature fluctuations W_T in a closed room and in open air.

To construct an abstract model $\Phi_T(\iota)$ of incipient turbulence spectra, the Karman model with roll-off corresponding to Fig. 5 within the inertial interval can be used. Such a crude model was obtained in Ref. 1:

$$\Phi_T(æ) = A_0 C_T^2 \, (6{,}6\, æ_0)^{2(\nu - 1/3)} \, (æ^2 + æ_0^2)^{-(\nu + 3/2)} \cdot \exp(-æ^2/æ_m^2), \qquad (1)$$
$$A_0 = 0.033,\ æ_0 = 2\pi / L_0,\ æ_m = 5.92 / l_0 .$$

where L_0 and l_0 are the outer and inner turbulence scales, respectively; $\nu = 1/3$ for the developed turbulence, then $\Phi_T(æ) \sim æ^{-11/3}$ in the inertial interval. According to Fig. 5, $\nu = 5/6$ in the incipient turbulence, hence, $\Phi_T(æ) \sim æ^{-14/3}$ in the most part of inertial interval. Further a more rapid spectrum roll-off is described by the exponential factor in Eq. (1). The parameters L_0 and l_0 for $\nu = 5/6$ and $\nu = 1/3$ are given in Table 1, from which it is evident that the inner scale of incipient turbulence l_0 (average $l_0 = 1.9$ cm, $\nu = 5/6$ and $l_0 = 2.7$ cm, $\nu = 1/3$) is one-order-of-magnitude larger than the inner scale in open air (0.7–4 mm[3,5,2]).

The spectrum $\Phi_T(æ)$ at $\nu = 5/6$, which can be considered as a n incipient turbulence spectrum, meets the experiment better that at $\nu = 1/3$ (developed turbulence spectrum, $\nu = 1/3$, but with L_0 and l_0 for incipient turbulence, Table 1). It is evident from the comparison of curves *4* and *5* in Fig. 5. Areas under these curves differ from experimental one by 15% ($\nu = 5/6$) and 28% ($\nu = 1/3$), respectively. However, model (1) with $\nu = 1/3$ is widely used; it allows one to transfer solutions of problems of wave propagation in the developed turbulence to the case of incipient one. Hence, this model is preferable.

The maximum error of spectrum approximation by Eq. (1) falls into the region of very large frequencies (viscous interval). Therefore, problems of wave propagation, where this interval is of great importance, require a more detailed model as compared to Eq. (1). The viscous interval does not significantly contribute into problems of optical beam shift, image jitter, etc., i.e., where wave phase fluctuations play a key part; therefore, equation (1) can be used here.

The size distribution of outer turbulence scale L_0 in vertical plane inside the pavilion is shown in Fig. 6. Periodic behavior of the inner scale l_0 is similar to those shown in Fig. 6 for the outer one (see Table 1). In this case, the smaller outer scale corresponds to the smaller inner one. It is known, that outer and inner scales determine maximum and minimum sizes of inhomogeneities. Hence, a spatial periodicity of sizes of temperature field inhomogeneities (of quincunx structure type) inside the pavilion follows from Fig. 6 and Table 1.

Table 1. Parameters of incipient turbulence spectra				
Observation point No.				
	ν = 5/6	ν = 1/3		
	L_0 cm	l_0 cm	L_0 cm	l_0 cm
1	33.2	1.2	83.0	1.8
2	47.4	2.3	101.6	3.5
3	19.8	1.2	53.9	1.2
4	27.0	1.8	67.5	2.8
5	62.6	2.3	125.1	4.1
6	18.5	1.6	46.4	2.1
7	46.4	2.3	126.5	2.9
8	18.0	1.84	36.0	2.8
9	60.3	2.3	139.2	3.9
10	18.1	1.8	38.9	1.8
11	30.4	2.3	76.1	2.9

1225.42.354.33.2

Regions with decreased outer scales can be called turbulence locks (or focuses), where intensified decomposition of the large-scale averaged flow to smaller spatial components is observed. The intensity of random temperature variations, characterized by the periodic parameter *C*, at average, decreases in the focuses, which is caused by smaller temperature differences (of passive admixtures[3,5]) in smaller vortices there.

1.3. STOCHASTIC SCENARIOS OF CONVECTIVE FLOWS

Compare the measurements in the pavilion with the well-known data on turbulence incipience from laminar flows (stochastic scenarios).

The most known stochastic scenarios are Landau–Hopf, Ruelle–Takens, Feigenbaum, and Pomeau–Menneville.[3] It will be shown below, that all these scenarios are confirmed in the incipient turbulence.

a) the Pomeau–Menneville scenario

As is known[3,4], as the distance increases (Reynolds number) in laminar flows in pipes, small turbulent regions with non-laminar flow first arise. These regions are usually called turbulent locks (or focuses). The locks become longer with increasing the distance and finally merge in a continuous turbulent flow. Turbulent locks are observed in experiments with other schemes as well[4]. The locks cause alternation of laminar and turbulent modes. Such turbulence incipience via alternation is called the Pomeau–Menneville scenario[3, 6].

It follows from our measurements, that turbulent locks and alternation (and, as follows from Fig. 3, the corresponding bifurcations of stability change) exist in periodic flows in the Benard cell as well. The parts of locks are played by regions with decreased spatial components (outer L_0 and inner l_0 scales). The locks turn out to be trapped in the structure of the Benard cell and alternate with regions of large L_0 and l_0 scales. Hence, our data confirm the Pomeau–Menneville scenario.

b) the Landau–Hopf scenario

The incipient turbulence in the Benard cell is a convenient model allowing one to trace the decomposition of energy-carrying vortices into smaller ones. In fact, the toroidal vortex of averaged movements can be considered as the only energy-carrying vortex in the Benard cell. Its sizes are determined by sizes of the room, where it originates. It is difficult to register the sizes of the main energy-carrying vortex in open air, because they depend on climate-forming factors. The outer turbulence scale is usually considered as this vortex, which itself is the decomposition product.

The correlation factor b_T and the sample non-smoothed temperature frequency spectrum W_T, calculated from the pavilion measurements data, are shown in Fig. 7. The correlation factor b_T has been calculated from different sample estimates[7–9], which, however, give no agreement between the results and reveal the local maxima of b_T. The correlation function can be calculated with an arbitrary small error at the large sample length N (a variance of b_T error is proportional to $1/N$). In our case, $N = 19139$; hence, the 95% confidence bound of b_T definition, shown in Fig. 7, makes $\pm$ 0.014; this is much less than b_T maxima.

The sample spectrum W_T was calculated without smoothing with a rectangular spectral window. As is known[7,8], such a window acts like a slit of about $2/T$ in width ($T = 120$ s). This resolution is sufficient to reveal the W_T spectrum maxima, uniquely corresponding to b_T maxima. Arguments of b_T and W_T maxima are related as $\tau_k f_k = 1$, $k = 1, 2,\ldots$ (τ_1 and f_1 usually determine characteristic scales of b_T and W_T decrease). The diameter of the main energy-carrying vortex $2R_1$ is easily retrievable from the relation $2\pi R_1 = \upsilon \tau_1 = \upsilon / f_1$; it is equal to 294.4 cm ($\upsilon = 9$ cm/s, $f_1 = 0.00973$ Hz) at point *5* in the pavilion. Virtually the same result is obtained from data of Fig. 2, if the trajectories of averaged movements are considered as circles.

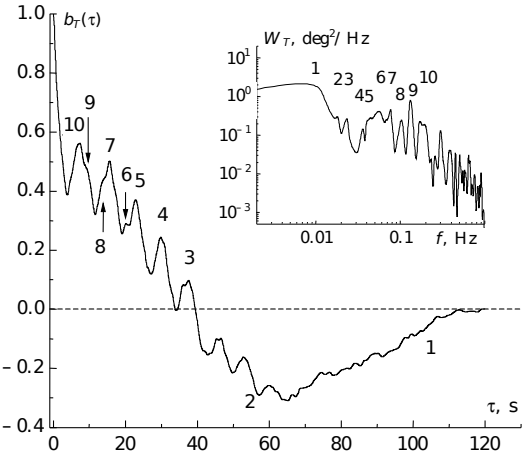

Fig. 7. Correlation factor b_T and non-smoothed frequency spectrum W_T (top right) in the pavilion. Figures designate the numbers of b_T and W_T maxima, corresponding to each other.

Comparison of W_T spectra in Figs. 5 and 7 shows disappearance of real spectrum maxima at a standard spectrum smoothing by a wide window (dispersion of the smoothed spectrum in Fig. 5 is equal to 1% of the sample spectrum dispersion in Fig. 7). Therefore, to calculate frequencies of spectrum maxima (harmonics), data of Fig. 7 are required. However, the rectangular spectrum window has large side lobes, causing oscillations especially at high frequencies. It is possible to get rid of these lobes using any of commonly used nonrectangular windows (difference between them is negligible), for example, the Welch window[9]. This window about two-fold decreases the dispersion as compared to a rectangular one and similarly widens the frequency band width. The widening is acceptable, because the bandwidth turns out to be less than the mean width of spectrum maxima. This is evident from data for W_T in Fig. 7.

To improve the sample estimate, a digital threshold filter can be used additionally to eliminate weak (lower than the averaged in Fig. 5) harmonics in spectrum. These harmonics can be interpreted either as high frequency side lobes, incompletely damped by the Welch window, or a weakly pronounced transient process of energy-carrying vortex decomposition to smaller ones. It is shown below (see Fig. 10), that the structure of weak harmonics is fractal, it does not coincide with those of side lobes. Therefore, the side lobes are completely damped. The level of the used threshold filter in the form of smoothed spectrum W_T (with 1% dispersion) has been chosen on the base of detailed analysis of sample spectra at many measurement points in the pavilion. The threshold filter is thus singles out main maxima (or first-order harmonics) from the spectrum.

Based on the above analysis, the frequencies of first-order harmonics (arguments of maxima) in the fluctuation spectrum W_T can be interpreted as frequencies of stable vortices observed in the temperature field (Fig. 8). The vortex frequencies f_n turn out to be multiple to the frequency of main energy-carrying vortex $f_1 = 0.00973$ Hz. Normalized to f_1, they are integer natural numbers ($n = 1, 2, \ldots$):

$$f_n/f_1 = 1, 6, 8, 11, 13, 17, 20, 66, 68, 77, 90, 93, 109, 113, 117, 120, 127, 130, 133, 136,$$
$$144, 150, 152, 157, 162, 164, 167, 175, 179, 183, \ldots.$$

Multiple frequencies is an exact result of discrete decomposition of the main energy-carrying vortex to smaller ones. The multiplicity means also that the phases of different harmonics (oscillations) are rigidly bound (agreed). In this case, the oscillations are called coherent (in-phase). Note that the function $f_n/(nf_1)$, shown in Fig. 8, is tolerant to variations of threshold filter level; it varies insignificantly at essential variations of the filter level.

Vortex diameters R_n (cm) for each harmonics can be calculated by the equation $2\pi R_n = \upsilon / f_n$, $n = 1, 2,\ldots$:

$$R_n = 147.21, 24.52, 18.39, 13.38, 11.32, 8.66, 7.36, 2.23, 2.16, 1.91, 1.63, 1.58, 1.35, 1.30, 1.26, 1.23,$$

1.16, 1.13, 1.11, 1.08, 1.02, 0.98, 0.97, 0.94, 0.91, 0.90, 0.88, 0.84, 0.82, 0.80, …

They are shown in Fig. 9. As shows the comparison of data in Fig. 9 and Table 1 (point *5*, $\nu = 5/6$), the second frequency $6f_1$ approximately corresponds to the outer turbulence scale L_0 ($2R_1 = 294$ cm, $2R_2 = 49$ cm), while the frequencies $127f_1$ and $130f_1$ (terminating the inertial interval) – to the inner one l_0 ($2R_{17} = 2.3$ cm).

Vortices, which are decomposition products of larger vortices (their frequencies are multiple to lower ones) are observed in the viscous interval and in a part of inertial one. For example,

$$f_n/f_2 = 11, 15, 20, 24, 25,\ldots (n = 8, 11, 16, 21, 22,\ldots); \quad f_n/f_3 = 15, 17, 18, 19, 36,\ldots (n = 16, 20, 21, 23, 52, \ldots).$$

The processes, observed inside the pavilion, are stable. Therefore, both the origination of vortex in the Benard cell (due to a temperature gradient) and its decomposition into smaller ones happen permanently (probably, with simultaneous self-replication). This evidently results in a threshold N-periodic flow with the frequencies f_n, $n = 1, 2, ..., N$. Transformation of a small perturbation into a stable periodic flow follows from solutions of the Landau equation; the origination of time-periodic flows is called normal Hopf bifurcation. The Landau–Hopf scenario describes the incipience of turbulence as a sequence of normal bifurcations, generating a limiting N-periodic flow ($N \gg 1$) with, generally speaking, incommensurable frequencies.

However, the frequency (phase) incommensurability is usually unrealizable (this is seen from our data as well). Therefore, to save idea, it is considered now that normal bifurcations generate consequent subharmonics[3, 11]. It is easily seen that our results confirm the Landau–Hopf scenario.

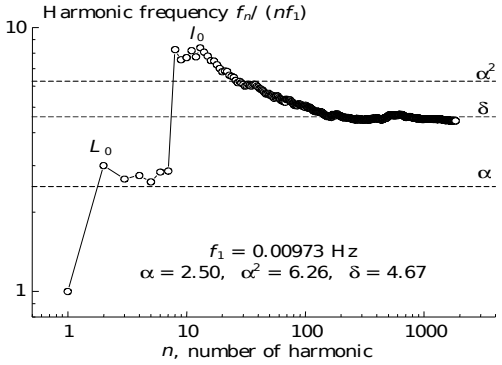

Fig. 8. Frequencies of the first-order stable vortices (harmonics) f_n in the fluctuation spectrum W_T

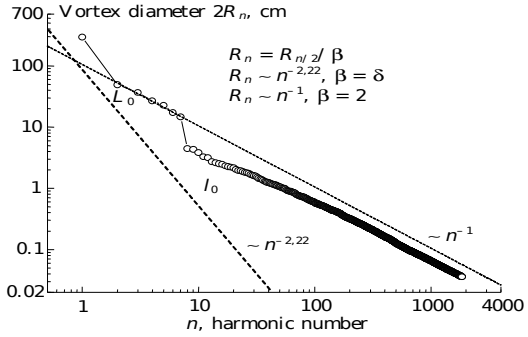

Fig. 9. Diameters of first-order stable vortices $2R_n$ in the fluctuation spectrum W_T

c) the Ruelle–Takens scenario

The Ruelle–Takens scenario can be considered as a refinement of the Landau–Hopf scenario. The difference is in the number of normal bifurcations, after which a flow can be considered as turbulent. According to the scenario, the turbulence occurs (a strange attractor appears) already after three normal bifurcations[3,10], i.e., a three-periodic flow ($N = 3$) can be already considered as turbulent. Then the convective flow becomes turbulent after origination of the main vortex in the Benard cell and two events of its decomposition.

d) the Feigenbaum scenario

The Feigenbaum scenario describes the turbulence incipience (appearance of a strange attractor) as a result of infinite consequence of period-doubling bifurcations[11]. These bifurcations appear only after magnitude change of a certain controlling parameter μ, e.g., Reynolds or Rayleigh numbers, etc. As is known, the Feigenbaum scenario follows from the universality of location of periodic points x_0, (x, x), (x, x, x, x), ... of 2^m-multiple cycles. These points x on the $x(\mu)$ curve correspond to tree branches, which symmetrically bifurcate at critical bifurcation points μ_m. Asymptotic similarity relations

$$= \{ \quad , \sigma_m(\mu) = = \delta \ , \alpha = 2.503, \delta = 4.669.$$

($m \gg 1$, α and δ are the Feigenbaum constants) are correct for both x and μ_m. Here x is usually (due to the universality) considered as the main parameter, characterizing a nonlinear dynamic structure, e.g., coordinates (in meters), or standard (m/s) or normalized speed (Hz = 1/s), as in the case of Navier–Stokes equations.

Though the equality $\sigma_m(\mu) = \delta$ is asymptotic, its suitability already after two–three period doublings (up to several percents) has been shown[11]. The theory has a high predictability due to the large rate of convergence δ ($\delta = 4.67$). For approximate evaluation, this equality can be used at $m \geq 0$. It is obvious that the equation $\sigma_m(\mu) = \delta$ has the solution $\mu_m = c\delta^{-m} + \mu_\infty$, c = const. Taking $m = 0, 1$ in the solution, we obtain a set of equations to find the constants c and μ_∞. Hence, $c = \mu_0 - \mu_\infty$ and $\mu_\infty = \mu_0 + (\mu_1 - \mu_0)\delta/(\delta - 1)$. As is known, one can take $\mu_0 = 1$ and $\mu_1 = 3$ for the logistic equation $x_{m+1} = \mu x_m(1 - x_m)$, considered in Ref. 11, hence, $\mu_\infty = 3.54508$, which insignificantly differs from the exact value $\mu_\infty = 3.56994$, obtained in Ref. 11. Note, that μ_m (at $\mu_\infty \geq 0$) can both increase ($c < 0$) and decrease ($c > 0$) with increase of m.

In our case, the value of the controlling parameter μ is fixed (pavilion sizes, temperature gradient, etc. are preset) and, hence, we can observe only products of vortex decomposition. Due to self-replicating of harmonics in the presence of doubling bifurcations, the harmonics, resulting from these bifurcations, are recordable.

Let, for example, the basic system parameter x be a shift with the length dimension. Then x_0 ($m = 0$) can be identified with the radius of the basic vortex R_1. The following variables (x, x) are to be the products of x_0 decomposition (nonsymmetrical bifurcation at $m = 1$). The only next largest radiuses R_2 and R_3 can play their parts (others are too small). Hence, as it follows from the decomposition diagram[11], the pairs R_4, R_5 or R_5, R_6 (the first element in each pair is approximately equal to a half of R_2 and the second – to a half of R_3) can be chosen as the pair x, x ($m = 2$). Substituting these variables in the Feigenbaum equation, we obtain $(R_2 - R_3)/(R_4 - R_5) = 2.97$; $(R_2 - R_3)/(R_5 - R_6) = 2.30$. Another pair x, x ($m = 2$) should be chosen from evident decomposition products of the vortices with radiuses R_2 and R_3 (their frequencies are multiple to f_2 and f_3); R_8 and R_{16} correspond to the first decomposition elements (see above). From the Feigenbaum equation, found $(R_2 - R_3)/(R_8 - R_{16}) = 6.11$. Thus, though we are at the top of bifurcation tree ($m = 1, 2$), the obtained values of the modulus of left part of Feigenbaum equation are close to α and α^2. Note, that R_n satisfy the equation $R_n = R_{n/2}/\beta$ (see Fig. 5); in the inertial and viscous intervals $\beta \approx 2$. However, $\beta \approx \delta$ in the energy interval and in the inertial one near l_0, hence, the equation $R_n = R_{n/2}/\delta$ agrees with the Feigenbaum similarity equation for the Fourier harmonics of x [Refs. 3 and 11].

The Feigenbaum constants α, α^2, and δ are best pronounced in the harmonic frequency plot. As it is seen from Fig. 8, the normalized frequency $y_n = f_n/(nf_1)$ undergoes two large jumps with the rise in n. The first jump is observed near the outer turbulence scale L_0 (as a result, the frequency y_n is saturated to the level α) and the second one – near the inner scale l_0 (y_n is saturated to the level δ bypassing the level α^2). These jumps correspond to large steps of the function f_n/f_1 which can be interpreted as an analog of the "devil's staircase" (see Fig. 10). The presence of α, α^2, and δ in Fig. 8 and the satisfaction the similarity equation confirm the Feigenbaum scenario.

Since $y_m \to \delta$ and $\sigma_m(\mu) \to \delta$ at $m \gg 1$, then bifurcation values of the controlling parameter μ_m can be connected with the harmonic frequencies f_m and vortex radiuses R_m, which are different parameters of the same turbulence incipience process. Actually, $|y_m - \delta| < \varepsilon$ and $|\sigma_{m^*} - \delta| < \varepsilon$ are should be true for some positive ε, δ_1, and δ_2 as soon as $m^* > \delta_1$ and $m > \delta_2$. Then $|y_m - \sigma_{m^*}| = |(y_m - \delta) - (\sigma_{m^*} - \delta)| \leq |y_m - \delta| + |\sigma_{m^*} - \delta| \leq 2\varepsilon$. Consequently, $\sigma_{m^*} \to y_m$. The levels δ_1 and δ_2 can be connected with each other, considering the domains of the confident convergence at sufficiently large m^* and m. It is known[3,11] that σ_{m^*} converges rapidly after several iterations, therefore, $m^* \approx 4$–5 can be taken as the domain of confident convergence. This determines the level δ_1. As is evident from Fig. 8, the frequency y_m rapidly converges to δ near the inner scale l_0 at $m \approx 17 \div 30$ (level δ_2). Hence, levels δ_1 and δ_2 and numbers m^* and m are approximately related as $\delta_2 \approx 2^{\delta_1}$ and $m \approx 2^{m^*}$.

Taking these relations into account and solving the equation $\sigma_m(\mu) = y_n$, where $n \approx 2^m$, obtain

$$\mu_m = c\, y_n^{-m} + \mu_\infty, \quad y_n = f_n/(n f_1) = \upsilon/(2\pi\, n f_1 R_n), \; c = const, \; n \approx 2^m. \tag{2}$$

The constant c is determined here after the choice of μ, for example, in the form of the Reynolds number Re, Rayleigh number Ra, or others. For approximate estimates, equation (2) and $\sigma_m(\mu) = \delta$ are applicable at $m \geq 0$.

As an example, we show how equation (2) can be used provided μ is the Rayleigh number. Let $\mu_m = Ra_m/\text{const}$ in Eq. (2). The new constant simply leads to the overdetermination of c.

Let us observe the decomposition process of the main vortex in the Benard cell to the level, when the existence of steady periodic flows (vortices) becomes impossible. In this case, the *Ra* number decreases from some maximum Ra_0 to the critical Ra_{cr}. In the process of decomposing, $Ra_m \ll Ra_{cr}$ at a sufficiently large *m* and, hence, Ra_∞ can be taken equal to zero in the first approximation. From Eq. (2), obtain then $Ra_m = Ra_{m0}\, y_{n0}^{\,m0}\, y_n^{\,-m}$, where m_0 is the *m* value, at which Ra_{m0} is known (since $n = 2^m$, then $n_0 = 2^{m0}$). If $m_0 = 0$, then, according to the Feigenbaum numeration, Ra_{m0} is the Rayleigh number for the main vortex in the Benard cell. This number can be roughly found, taking the layer thickness *h* in *Ra* definition equal to the main vortex diameter.

The bifurcation diagram of the main vortex decomposition in the Benard cell is shown in Table 2 (the dependence of Ra_m numbers on the bifurcation number *m*), as well as the harmonic numbers *n* and vortex diameters $2R_n$ (cm) corresponding to *m*. As is seen from Table 2, the bifurcation numbers Ra_m decreases with the rise of *m* and cross the level Ra_{cr} ($Ra_{cr} = 657 \div 1708$) at $m = m_{cr} \approx$ 9–10. The same m_{cr} value is obtained from the number of the recorded harmonics (in Fig. 8, the maximal *n* equals 1849): $m_{cr} \approx E(\log n / \log 2) = E(10.85) = 10$, where $E(x)$ is the integer part of *x*.

Thus, the origination of the main vortex in the Benard cell and about ten events of its discrete decomposition are observed in the pavilion. Vortex diameters, corresponding to the critical values m_{cr} (see Table 2), are within the 0.6–1.2 mm range. They agree with sizes of minimal vortices, existing in air[3].

Table 2. Bifurcation diagram in main vortex decomposition

m	*n*	Ra_m	$2R_n$, *cm*
0	1	$1.55 \cdot 10^9$	294
1	2	$5.15 \cdot 10^8$	49.1
2	4	$2.05 \cdot 10^8$	26.8
3	8	$2.76 \cdot 10^6$	4.5
4	16	$4.89 \cdot 10^5$	2.5
5	32	$1.94 \cdot 10^5$	1.5
6	64	$6.86 \cdot 10^4$	0.87
7	128	$2.65 \cdot 10^4$	0.50
8	256	$9.46 \cdot 10^3$	0.26
9	512	1474.1	0.12
10	1024	444.7	0.06
11	2048	67.5	0.05

On the base of the performed analysis, the known stochastic scenarios can be divided into two groups. The first one includes scenarios of origination of periodic flows from laminar ones. Among these scenarios are, first of all, Pomeau–Menneville and Rayleigh–Benar convection. The second group includes decomposition scenarios (degeneration) of the appeared vortex periodic flows, the main of them is the Feigenbaum scenario. The Landau–Hopf and Ruelle–Takens (origination of the limiting *N*-periodic flow) scenarios contain features of both groups.

It follows from the obtained results, that scenarios of both groups are confirmed in the incipient turbulence, a periodic flow originates (the main vortex in the Benard cell) and discretely decomposes. These processes in principle (in the simplest situations) are confirmed by known solutions of nonlinear equations of hydrodynamics. However, such solutions for a general case are presently unknown. It is clear, that vortex solutions should exist, since they are experimentally observed. It is also clear, that the stability of vortex solutions will be determined by nonlinear resonances (both between external forces and dissipative processes and between harmonics with commensurable frequencies). Therefore, the mechanism of hydrodynamic turbulence incipience and existence becomes clearer, in which the role of stochastization essentially decreases. Then the turbulence, usually considered as a merely random event, turns to be significantly determinate.

The turbulence determinacy is much stronger than it could be expected from the above analysis. Actually, it follows from the consideration of the threshold-filter damped spectrum harmonics W_T in Fig. 3, that their greatest maxima (second-order harmonics) can be extracted with the same filter. It turns out that the local structure of second-order harmonics location (between the neighboring first-order ones) is similar to the structure of first-order harmonics location throughout the spectrum W_T. The local self-similarity of the spectrum or, in other words, the fractal structure of the turbulence spectrum is observed.

The frequency dependence of the first- and second-order harmonics (normalized frequencies f_n / f_1 of harmonics) is shown in Fig. 10. This dependence is usually called the "devil's self-similar staircase" [12–14]; here each inner space between main steps is similar to the whole staircase. Each dash (step) answers its f_n / f_1 value (all these values are integers in Fig. 10). Long dashes correspond to first-order harmonics and short dashes – to second-order ones.

The distances between arguments of the neighboring harmonics $f_n - f_{n-1}$ ($n = 2, 3, \ldots$) as functions of frequency (of frequencies f_n) are shown in Fig. 11. The bottom plot here shows the distances between the arguments of first-order harmonics for the whole spectrum W_T (see Fig. 7). (As is seen from Fig. 5, it is sufficient to consider only the 0–10 Hz frequency range in the spectrum W_T, without weak noise component, which is caused by the transfer of the motion energy to heat (and the hardware errors also) and is observed at frequencies higher than 10 Hz.) The middle plot in Fig. 1 shows the distances between arguments of second-order harmonics for the longest range between the first-order harmonics (0.19–0.64 Hz) and the upper one – for the 23.34–23.44 Hz range. As is seen from the "devil's staircase,"

other ranges contain a less number of second-order harmonics (because of limited experimental facilities) and, hence, are not so convenient for the analysis.

The comparison of the data in Fig. 11 confirms a similarity of locations of the local structures of second-order- and first-order-harmonics in the whole spectrum W_T. The devil's staircase is truly self-similar and the spectrum is fractal. Since second-order maxima are significantly weaker than first-order ones, the second-order harmonics can be called the fractal shadows of the first-order ones. Thus, the process of turbulent flows originating and decomposing is evidently determinate even in weak spectral particulars.

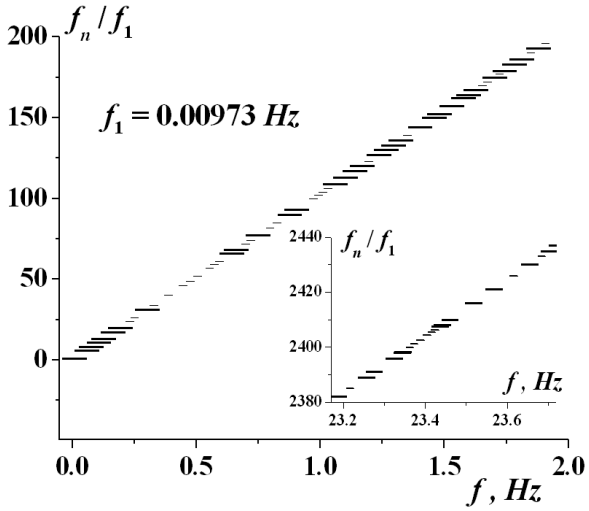

Fig. 10. "Devil's self-similar staircase" (normalized frequencies of the first- and second-order harmonics f_n/f_1). The fragment shows the devil's staircase in the 23.1–23.7 Hz range

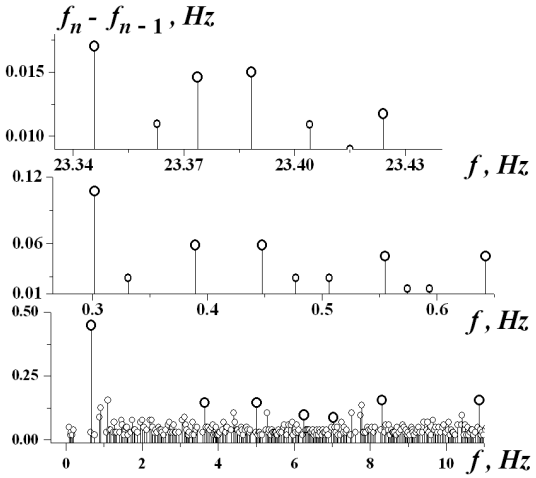

Fig. 11. Distances between neighboring harmonics $f_n - f_{n-1}$ (n = 2, 3, ...): between the first-order harmonics of the whole (bottom plot), second-order one for the 0.19–0.64 Hz (middle plot) and 23.34–23.44 Hz (upper plot) ranges

The conditions of chaos occurrence in typical dynamic systems, laid down in Refs. 12–14, allows one to point out the characteristic universal features observed in turbulence origination (in incipient turbulence), such as[12]: origination of irregular long-living spatial structures, form (character) of which is determined by dissipative factors, local instability and fractal character of phase space of such structures, appearance of central (on zero frequency) spectral peak.

All these features are observed in our measurements. A convective Benard cell is a spatial structure; its form depends on medium viscosity and space geometry (form), where it originates (dissipative factors). The cell is locally unstable and cascade decomposes to smaller ones (vortices). The passive admixture spectrum (temperature) in the cell is fractal. The average temperature is not constant due to nonstationarity of a random process in the cell (bifurcation of stability change, see Fig. 3). Without additional actions for elimination of the nonstationarity (average value of random function is obtained by time averaging over the length of characteristic scale of function variation, but not over the whole sample) the centered random temperature includes a non-compensated constant component. Just this component raises the low-frequency part of Fourier spectrum and gives the central peak on zero frequency. Such phenomenon is observed for the Fourier transform of both correlation and the random nonstationary function.

It is convenient to name the above features "coherent structure". A.S. Monin and A.M. Jaglom[3] define a coherent structure as a random nonlinear superposition of considerably stable large-scale turbulence components. According to the above results, we can define a coherent structure as following. A hydrodynamic coherent structure is a compact formation containing a long-lived spatial structure, resulting from long-term action of thermodynamic gradients, and products of its discrete coherent cascade disintegration.

The disintegrating spatial structure can be called a cell (structure) generating a coherent structure. Disintegration of the generating cell is accompanied by origination of the main energy-carrying vortex. The frequency of this main vortex can be considered as the main features of both generating cell and the coherent structure. Sizes of the coherent structure are fuzzy. Flows, external with respect to the generating cell, can transport products of its disintegration to significant distances, forming long turbulent wake. The lifetime of a coherent structure is determined by the action time of thermodynamic gradients. As a limit case of very weak local instability (when a generating structure is locally stable and does not disintegrate), a coherent structure can consist of only one long-living generating structure. In this case, the generating structure is some configuration of laminar flow. Such situation we have when observing, for example, Benard cells in a thin layer of very viscous liquid.

Thus, the process of turbulence incipience can be connected with origination of coherent structures. The compact formation, observed in our experiments, includes a long-living main energy-carrying vortex and products of its simultaneous cascade discrete decomposition (coherent vortices with multiple frequencies). The main vortex frequency is determined by convective Benard cell sizes. According to our definition, such formation is a coherent structure.

Origination of coherent structures in liquid, e.g., in water, is of interest. An example of smoothed turbulence spectrum in ocean is given in Ref. 3. This spectrum, similar to those in a coherent structure in air (see Fig. 5), has echelon frequency ranges with 5/3 decrease. The echelon structure of such spectrum allows it to be considered as the spectrum of coherent structure in water.

Flows in pipes easily yield to experimental investigation. However, they are studied not enough theoretically. In this case it is clear from qualitative consideration that the pressure gradient P in liquid can play the part of temperature gradient required for convective cell origination. This follows already from the simplest equation of state $P = const\ \rho\ T$. The density of incompressible liquid ρ is usually considered as constant, hence, $P \sim T$. Therefore, cells similar to convective can appear in liquid in presence of the long-living pressure gradient. Disintegration of these cells should generate a coherent structure. In contrast to the Rayleigh–Benard convection, vertical sizes of flows in pipes (pipe length) essentially exceed horizontal ones (pipe cross-section). Therefore, cells are situated not horizontally, but vertically, i.e. along the pipe length. In addition, there is a middle flow. It distorts the cell form and transport disintegration products of generated cells (smaller vortices) to the orifice, where they accumulate and a segment of continuous turbulence (commonly called developed) appears. This situation is described by the stochastic scenarios via alternation.

Similar patter arises in flowing different obstacles, which follows from data of numerous observations. A long-living main vortex (generating structure, sometimes several) originates on the obstacle surface (near the backwall). Clear large vortices appear behind the obstacle (at some distance); they are not larger than the main one. The shape of vortices is distorted by an external flow (front surface is indented). At further moving off, several smaller vortices are observed and again continuous turbulent flow. Absence of tight bounds (e.g., pipe walls) results further in transversal flowing of turbulent wake. The described phenomenon is the result of transport of generating structure disintegration products by the external flow. This is a coherent structure.

2. COHERENT STRUCTURES IN OPEN AIR

As is known from meteorology, sufficiently stable vortex formations (cells) of different scales exist in the atmosphere. The Ferrel and Hadley cells are the largest among them (up to 5000 km in radius). They can be considered as modifications of Benard cells in a thin spherical layer (at the Earth scale). Somewhat smaller cells (cyclones, anticyclones, thunder-cells, tornados, etc.) exist there as well. The decomposition products of these vortices have clearly pronounced deterministic character (corresponding to a coherent structure or the non-Kolmogorov incipient turbulence) and are observable in open air.

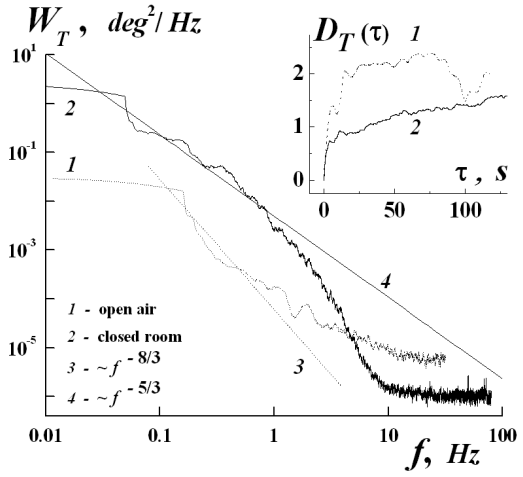

Fig. 12. Kolmogorov turbulence is the result of mixing of different coherent structures. W_T are the smoothed spectra; D_T is the structure functions of temperature fluctuations: curve *1* corresponds to summer daytime measurements in mountains (at a height of 2032 m). curve *2* corresponds to wind transfer of a frozen spatial pattern of flows inside the LSVT through one point

Open-air measurement data (The Sayan Solar Observatory, July 5, 2007) are shown in Fig. 12 along with the modeled results of the steady-wind transfer of a frozen spatial pattern of flows inside the LSVT (sequential slow transfer of data, recorded at seven abreast neighboring points, located along a straight line at one height[1], through point *5*, Fig. 1). This straight line includes not only points *5*, *4*, and *2* in the spectrograph pavilion, but also another four points, located in neighboring closed LSVT rooms, which are isolated from the pavilion. Frequencies of main energy-carrying vortices are different in these rooms and the pavilion. Comparison of Figs. 12, 5, and 4 shows that the results for open air, given in Fig. 12, indicate the prevailing activity of one coherent structure ($W_T \sim f^{-8/3}$ within the inertial interval). On the contrary, transfer of determinate vortices, formed inside closed rooms, through one point results in the turbulence close to Kolmogorov ($W_T \sim f^{-5/3}$). Hence, the conclusion can be drawn that the real atmospheric Kolmogorov turbulence is a mixture of determinate vortices from different

coherent structures. Inequality (non-multiplicity, incommensurability) of frequencies of main vortices of different coherent structures results in out-of phase (non-coherent) oscillations which are disintegration products. Hence, is naturally to call the turbulence, originating in mixing of coherent structures with incommensurable frequencies of main vortices, non-coherent.

As a result of expeditionary works in mountain and flat conditions in 2000th years, the authors gather an extensive experimental database of surface measurements of main turbulence parameters in various geographical areas and meteorological situations. It follows from the data that extensive areas, where one coherent structure exercises a decisively influence, are observed in open air. Moreover, characteristic features of coherent structures (coherent turbulence) are present in the majority of gathered data. The Kolmogorov non-coherent developed turbulence usually appears only over large areas with flat and uniform underlying surface.

The coherent turbulence differs from non-coherent one, first of all, in more rapid roll-off of the smoothed spectrum W_T in the inertial interval ($\sim f^{-8/3}$) and less contribution of high-frequency component (small-scale vortices). Therefore, in air, the spectrum in the inertial interval has two pronounced decrease regions within the areas with decisive influence of one (local) coherent structure, i.e., first a sufficiently rapid decrease is observed (usually $\sim f^{-8/3}$, sometimes even more rapid), and than the decrease slows down ($\sim f^{-5/3}$) with frequency rise. The second Kolmogorov region is characterized by a mixture of disintegration products of other large generating structures existing in the atmosphere. Sometimes the inertial interval of the spectrum has two pronounced stepwise regions with the 8/3-decrease. In this case, one can tell about presence of two local coherent structures in the measurement site.

Due to a difference of atmospheric coherent turbulence from the Kolmogorov non-coherent one, the Kolmogorov–Obukhov law applicability limits are to be specified. In particular, the values of Kolmogorov C and Obukhov C_θ constants are to be verified.

In accordance with the Kolmogorov–Obukhov law, the structure function of longitudinal velocity fluctuations $D_{rr}(r)$ in the inertial interval of the scales r is expressed via the structural characteristic C_V^2 of longitudinal velocity fluctuations: $D_{rr}(r) = C_V^2 r^{2/3}$. The structure function of temperature fluctuation $D_T(r)$ is expressed via the structural characteristic C_T^2 of temperature fluctuations: $D_T(r) = C_T^2 r^{2/3}$. The structural characteristics C_V^2 and C_T^2 determine the intensity of velocity and temperature fluctuations and are important parameters of medium turbulent motion. In their turn, C_V^2 and C_T^2 depend on the average dissipation rate of kinetic energy ε and temperature N and Kolmogorov C and Obukhov C_θ constants: $C_V^2 = C\varepsilon^{2/3}$, $C_T^2 = C_\theta \varepsilon^{-1/3} N$. Hence, velocity and temperature fluctuations are to be functions of C and C_θ at known ε and N. The constants C and C_θ were measured in different media by different methods. The values $C = 1.9$ and $C_\theta = 3.0$ are recommended[3] as the most probable estimates of the constants. This estimate is average with respect to data of different authors. Deviations from the average value are sufficiently large[3], e.g., the values 0.9, 1.6, and 2.8 were observed for C and 1.1, 1.4, 2.5, 2.7, 3.3, 3.5, 5.6, 5.8, 6.5, 9.0 – for C_θ .

As is known[3,5], the Kolmogorov constant C is related with the asymmetry S of probability distribution of longitudinal velocity difference of by the equation $C = (0.8/|S|)^{2/3}$, $S = D_{uuu}/|D_{uu}|^{3/2}$. The third moment of longitudinal difference of wind velocities $D_{uuu}(\boldsymbol{r}) = \langle [u'(\boldsymbol{r}'+\boldsymbol{r},t) - u'(\boldsymbol{r}',t)]^3 \rangle$ can be obtained from the time moment $D'_{uuu}(\tau) = \langle [u'(\boldsymbol{r}',t+\tau) - u'(\boldsymbol{r}',t)]^3 \rangle$ and the frozen condition[3] $D_{uuu}(\mathbf{v}\tau) = D'_{uuu}(\tau)$. Here $u'(\boldsymbol{r},t) = u(\boldsymbol{r},t) - \langle u(\boldsymbol{r},t)\rangle$, where $u(\boldsymbol{r},t)$ is the random value of longitudinal velocity (usually the projection of random velocity vector to the vector of average velocity) at the point $\boldsymbol{r}$ at the moment t. The constant C_θ is related with the asymmetry S of probability distribution of longitudinal temperature difference by the equation[3,5] $C_\theta = -(4/3)/(C^{1/2}S')$, $S' = D_{uTT}/(D_{uu}^{1/2}D_T)$. The third spatial moment of difference $D_{uTT}(\boldsymbol{r}) = \langle [u'(\boldsymbol{r}'+\boldsymbol{r},t) - u'(\boldsymbol{r}',t)]\,[T'(\boldsymbol{r}'+\boldsymbol{r},t) - T'(\boldsymbol{r}',t)]^2 \rangle$ can also be found from the time moment $D'_{uTT}(\tau) = \langle [u'(\boldsymbol{r}',t+\tau) - u'(\boldsymbol{r}',t)]\,[T'(\boldsymbol{r}',t+\tau) - T'(\boldsymbol{r}',t)]^2 \rangle$ and the frozen condition $D_{uTT}(\mathbf{v}\tau) = D'_{uTT}(\tau)$. Here $T'(\boldsymbol{r},t) = T(\boldsymbol{r},t) - \langle T(\boldsymbol{r},t)\rangle$, $u'(\boldsymbol{r},t) = u(\boldsymbol{r},t) - \langle u(\boldsymbol{r},t)\rangle$ is the centered random temperature and longitudinal velocity.

The process of Kolmogorov C and Obukhov C_θ constants determination is shown in Figs. 13 and 14 for the case of atmospheric non-Kolmogorov turbulence. The frequency spectrum, shown in Fig. 13, have a long inertial interval, where $W_T \sim f^{-8/3}$.

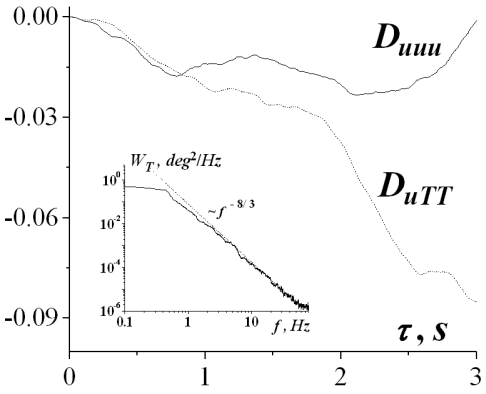

Fig.13. Third moments of longitudinal differences of velocities and temperatures D_{uuu} (m^3/m^3) and D_{uTT} (deg^2 m/s). The smoothed spectrum is shown in the fragment. Coherent turbulence, summer daytime measurements in mountains at a height of 680 m, July 2, 07

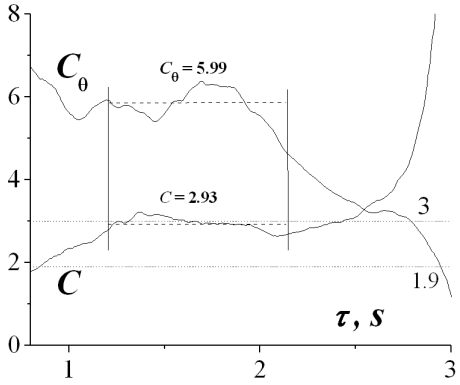

Fig.14. The Kolmogorov C and Obukhov C_θ constants. Coherent turbulence, measurements in mountains at a height of 680 m, July 2, 07. Vertical lines show the boundaries of the inertial interval, dashed lines – average values of C and C_θ

Analyzing more than 30 observation points, the following has been ascertained. If turbulence is close to Kolmogorov (flat underlying surface, time spectra in the inertial interval $W_u(f) \sim f^{-5/3}$ etc.), then C can be taken equal to 1.9 with an accuracy of 1–12 % and C_θ – to 3.0 with an accuracy of not worse than 30%. If the turbulence deviates from Kolmogorov and close to coherent ($W_u(f) \sim f^{-8/3}$ etc.), then C is within the 0.9–3.7 range and C_θ is within the 1.3–5.1 range. In this case, C = 1.9 with an accuracy of 19–93%, while the error of C_θ = 3.0 can reach 70%.

As follows from experience, atmospheric turbulent parameters measurement errors are usually significant. The main reason of these errors is clear from our measurement data. Variations of the Kolmogorov and Obukhov constants within 100% (depending of observation point) result in similar errors in determination of the characteristics C_T^2, C_V^2, and C_n^2.

Another reason of errors is the structure function of temperature fluctuations $D_T(r)$, if C_T^2 is found using the Kolmogorov–Obukhov law $D_T(r) = C_T^2 r^{2/3}$. As is known[5], the function $D_T(r)$ is representable as

$$D_T(r) = 8\pi \int_0^\infty d\,æ\,[1 - sin(ær)/(ær)]\,\Phi_T(æ)\,æ^2.$$

Substitute spectrum (1), written in exponential form:

$$\Phi_T(æ) = A_0\,C_T^2\,(6.6\,æ_{0e})^{2(\nu-1/3)}\,æ^{-2(\nu+3/2)}\,exp(-æ^2/æ_m^2)\;[1-exp(-æ^2/æ_{0e}^2], \qquad (3)$$
$$æ_{0e} = 2\pi/L_{0e}, \quad \nu = 5/6,\ 1/3.$$

Spectrum (3) differs from (1) only in its behavior in the energy interval, where $æ^2/æ_0^2 << 1$. There is a correlation between the Karman outer scale L_0 and exponential L_{0e} (usually L_{0e} = 0.54 L_0), when spectrum (3) gives the results similar to Karman (1). At the same time, it significantly simplifies calculations. After calculating the corresponding integrals, obtain asymptotic representations for the structure function $D_T(r)$ in coherent turbulence (ν = 5/6):

$$D_T(r) = 53.45 C_T^2\,L_0^{-1}\,l_0^{-1/3}\,r^2, \qquad r \ll l_0,$$
$$D_T(r) = C_T^2 r^{2/3} f(r/L_0),\ f(x) = 49.87\,(x - 1.34\,x^{4/3}), \qquad l_0 \ll r \ll L_0,$$
$$D_T(r) = 3.56 C_T^2\,L_0^{2/3}[1 - 0.63(r/L_0)^{-1/3}], \qquad L_{0e} \ll r.$$

The function $D_T(r)$ evidently deviates from the Kolmogorov–Obukhov "2/3" law. $D_T(r) \sim r^2$ at small r ($r \ll l_0$) like in the Kolmogorov turbulence; however, the asymptotic coefficient becomes dependent on the outer scale L_0. There is an extended initial region in the inertial range ($l_0 << r << L_0$), where $D_T(r) \sim r^{5/3}$. The regions $\sim r^2$ and $\sim r^{5/3}$ intersect at $r = 0.8\,l_0$ (remind here that the inner scale l_0 of the coherent turbulence is one order of magnitude larger than those of the Kolmogorov one). The function $f(x)$ has a maximum; therefore, a 2/3 Kolmogorov region, where $D_T(r) \approx C_T^2 f_{max}\,r^{2/3}$, is approximately observed in the inertial range of coherent turbulence 3.0 $l_0 \le r \le$ 0.4 L_0, where $f(x) \approx const = f_{max} = 2.17$. Hence, when measuring C_T^2 from the 2/3-asymptotics of $D_T(r)$, the values are more than two-time overestimated.

REFERENCES

1. Nosov V.V., Grigoriev V.M., Kovadlo P.G., Lukin V.P., Nosov E.V., Torgaev A.V., Astroclimate of specialized rooms of the Large solar vacuum telescope. P. 1.; P. 2 // Atmos. Ocean. Opt. V. 20, No. 11. P. 1013–1021 (2007); V. 21, No. 3. P. 207–217 (2008).
2. Nosov V.V., Emaleev O.N., Lukin V.P., Nosov E.V., Semiempirical hypotheses of the turbulence theory in the anisotropic boundary layer // Atmos. Oceanic Opt. **18**, No. 10, 756–773 (2005).
3. Monin A.S., Jaglom A.M. Statistical hydromechanics. V. 1. Nauka, Moscow, 1967, 696 pp.; V.2. Gidrometeoizdat, St.-Petersburg, 1996, 742 pp. (in Russian). Engl. Transl. (revised). MIT Press, Cambridge, Mass, 1977.
4. Zhigulev V.N. and Tumin A.M. *Turbulence Origination.* Nauka, Novosibirsk, 1987, 283 pp, (in Russian).
5. Tatarskii V.I. *Wave propagation in turbulent atmosphere*. Nauka, Moscow, 1967, 548 pp. Engl. Transl.: *The Effects of the Turbulent Atmosphere on Wave Propagation*. Israel Program for Scientific Translations, 1971, 472 pp.
6. Pomeau Y. and Menneville P., *Intermittent transition to turbulence dissipative dynamical system //* Comm. Math. Phys., v. 74, No 2, 1980, p. 189-197.
7. Jenkins G. and Watts D. *Spectral Analysis and its Applications*. Holden-day, San Francisco, 1968, 525 pp. Rus. Transl.: (Mir, Moscow, 1971), P. 1, 317 pp; (Mir, Moscow, 1972), P. 2, 285 pp.
8. Bendat J.S. and Piersol A.G. *Random Data: Analysis and Measurement Procedures*. Wiley, New York, 1971, 566 p.
Bendat J.S. and Piersol A.G. Measurement and analysis of random data. Wiley, New York, 1966, 390 p.
9. Press W. H., Teukolsky S. A., Vetterling W. T., Flannery B. P. *Numerical Recipes in C*. 2-nd ed. - Cambridge univer. press, 2002, 994 p.
10. Ruelle D., Takens F. *On the nature of turbulence* // Comm. Math. Phys., v.20, No 2, 1971, p. 167-192. Ruelle D. *Strange attractors* // Math. Intellengencer . v.2, No 3, 1980, p. 126-137.
11. Feigenbaum M. J. *Quantitative universality for a class of nonlinear transformations //* J. Stat. Phys., 19, No. 1, 1978, p.25-32. Feigenbaum M. J. Universal behavior *in nonlinear systems*. // Los Alam. Sc. v. 1, No. 1, 1980, pp. 4-27., Rus. Transl.: Usp.phis.nauk, v. 141. iss. 2. 1983. p. 343-374.
12. Zaslavskii G.M., Sagdeev R.Z. *Introduction in nonlinear physics: From pendulum to turbulence and chaos.* Moscow, Nauka, 1988, 368 pp.
13. Zaslavskii G.M. *Stochasticity of dynamic systems.* Moscow, Nauka, 1984.
14. Shuster G.G. *Deterministic Chaos. An Introduction.* Physik-Verlag. Weinheim. 1984. Rus. Transl.: Moscow, Mir, 1988, 240 pp.